Grant Title: Collaborative Research: Cloudiness transitions within shallow marine clouds near the Azores

Reporting period: 9/15/2011–9/14/2016
Funding period: 9/15/2011–9/14/2016
Report created: 1/15/2017

PI: David B. Mechem
University of Kansas
Atmospheric Science Program
Department of Geography and Atmospheric Science
1475 Jayhawk Blvd, 215 Lindley
Lawrence, KS 66045
Grant Number: DOE ASR DE–SC0006736

Collaborating PI: Simon P. de Szoeke
Oregon State University
College of Earth, Ocean, and Atmospheric Sciences
104 CEOAS Admin Building
Corvallis, OR 97331
Grant Number: DOE ASR DE-SC0006994

Collaborating PI: Sandra E. Yuter
North Carolina State University
Department of Marine, Earth, and Atmospheric Sciences
Campus Box 8208
Raleigh, NC 27695
Grant Number: DOE ASR DE-SC0006994

Project Summary

Marine stratocumulus clouds are low, persistent, liquid phase clouds that cover large areas and play a significant role in moderating the climate by reflecting large quantities of incoming solar radiation. The deficiencies in simulating these clouds in global climate models are widely recognized. Much of the uncertainty arises from sub-grid scale variability in the cloud albedo that is not accurately parameterized in climate models. The Clouds, Aerosol and Precipitation in the Marine Boundary Layer (CAP–MBL) observational campaign and the ongoing ARM site measurements on Graciosa Island in the Azores aim to sample the Northeast Atlantic low cloud regime. These data represent, the longest continuous research quality cloud radar/lidar/radiometer/aerosol data set of open-ocean shallow marine clouds in existence. Data coverage from CAP–MBL and the series of cruises to the southeast Pacific culminating in VOCALS will both be of sufficient length to contrast the two low cloud regimes and explore the joint variability of clouds in response to several environmental factors implicated in cloudiness transitions.

Our research seeks to better understand cloud system processes in an underexplored but climatologically important maritime region. Our primary goal is an improved physical understanding of low marine clouds on temporal scales of hours to days. It is well understood that aerosols, synoptic-scale forcing, surface fluxes, mesoscale dynamics, and cloud microphysics all play a role in cloudiness transitions. However, the relative importance of each mechanism as a function of different environmental conditions is unknown.

To better understand cloud forcing and response, we are documenting the joint variability of observed environmental factors and associated cloud characteristics. In order to narrow the realm of likely parameter ranges, we assess the relative importance of parameter conditions based primarily on two criteria: how often the condition occurs (frequency) and to what degree varying that condition within its typically observed range affects cloud characteristics (magnitude of impact given the condition). In this manner we will be able to address the relative importance of individual factors within a multivariate range of environmental conditions. We will determine the relative roles of the thermodynamic, aerosol, and synoptic environmental factors on low cloud and drizzle formation and lifetime. We will use the combined Azores and Southeast Pacific data set to address the following questions:

1. What are the key environmental factors governing the occurrence of drizzling and non-drizzling marine low clouds?
2. What are the key mechanisms governing transitions among mesoscale cloud structures?

These questions have relevance in understanding the physics underlying variations in top-of-atmosphere radiative properties of marine low clouds and potentially in prioritizing refinements in cloud parameterizations in global climate models.

Note that this final report summarizes the research efforts in which PI Mechem and his research group were direct participants.

Accomplishments

Characterizing synoptic and cloud-system variability over the Azores

The ARM Mobile Facility (AMF) deployment on Graciosa Island in the Azores during 2009–2010 demonstrated that the Northeast Atlantic exhibits a striking amount of variability in cloud system behavior. The variability over the NEA suggests questions like, "How much time does the region exhibit an environment characteristic of stratocumulus (or trade cumulus)? We have focused on the following objectives:

- Identifying preferential synoptic states over the NE Atlantic
- Projecting cloud system properties onto these synoptic states and quantifying the variability in these properties

We apply the technique of self-organizing maps (SOMs), an unsupervised artificial neural network learning technique, to characterize variability in synoptic conditions and cloud properties. The SOMs analysis produces from input data a finite number of characteristic patterns, for example the preferential synoptic configurations present in the input data. ERA–Interim reanalysis provided the input data for the SOM routine, representing years 1979 to 2012. In our preliminary analysis, the characteristic patterns (nodes) were constructed from 500-mb geopotential height data for all July dates corresponding to 0000 UTC, though in principle the SOM algorithm could be applied to any field. We specifically focus on the joint variability between different meteorological variables.

Figure 1 shows the mean 500-mb geopotential height field (ERA–Interim) for January and June. In June, the 500-mb level is characterized by weak height gradients, with zonal flow or slight ridging over the Azores region. January exhibits tighter gradients and stronger flow, with a pronounced trough the west.

We chose 25 nodes (a 5×5 map) for the SOM computation, which was run on the 500-mb geopotential height anomalies. Analysis is based on 500-mb heights because of its first-order importance in characterizing synoptic variability and association with properties like vertical motion, frontal patterns, and precipitation. The SOM nodes calculated for June are presented in Figure 2 as the positive (solid lines) and negative (dashed lines) mean anomalies for the data times mapped to each specific node. Overlaid on the anomalies are the mean 500-mb geopotential heights mapped to each node (we refer to these as "projected" or "composited" quantities). The SOM node space spans continuum of anomalies ranging from almost entirely positive values (node 15), half positive and negative (nodes 23 and 3) and nearly all negative (node 11). The relative frequency values for each node (Fig. 2) indicate that these archtypal nodes tend to exhibit the highest frequencies among all the nodes. The middle node (13) is characterized by a nearly uniform zero anomaly and may be interpreted as being close to the climatological mean. Typically, successive 500-mb fields in time exhibit a trajectory in node space around the edge states of the SOM, corresponding to an evolution of the synoptic pattern (not shown).

Means of the composited 500-mb geopotential heights for each node promote a meteorological interpretation of the SOM nodes. Positive anomaly structures correspond to heights greater than climatology but not necessarily a ridge-like structure. Note that the near-zero anomaly state (node 13) corresponds to a structure slightly perturbed from simple zonal flow, with the Azores lying just east of a weak ridge axis and just very west of a weak trough axis. Nodes 15 and 11 are characterized by ridge and trough axes, respectively, centered over the Azores. The Azores lie in a region of strong 500-mb

geopotential height gradients in two other very frequent nodes (23 and 3). We denote these nodes as archtypal "pre-trough" (node 23) and "post-trough" (node 3) patterns determined by the location of the trough axis relative to the Azores. Though the geopotential heights over the analysis domain rarely drop below 5400-m in June, the Azores regularly experience the influence of synoptic activity (e.g., nodes 16, 11, and 6). These nodes represent an intrusion of synoptic low-pressure systems over the Azores.

Based on the position of the 500-mb ridge and trough axes relative to the Azores, for each month we further cluster each node into different synoptic categories. Although objective methods for classifying SOM nodes exist (e.g., Vesanto and Alhoniemi 2000), we classify the 25 nodes by hand based on the 500-mb geopotential heights and anomalies, using our understanding of the structure of midlatitude synoptic systems.

Figure 3 shows these dominant synoptic states along with other projected environmental variables, specifically 1000-mb geopotential heights, 500-mb vertical velocity, and EIS. The pre-trough pattern shows that the Azores lie in a tight gradient of 500-mb heights, with the trough axis near the western portion of the domain. At 1000-mb, a weak Bermuda High is present south and east of the Azores, and a low-pressure center is present in the north- west portion of the domain. This 1000-mb trough is roughly co-located with the 500-mb trough axis. The Bermuda High is least dominant in this synoptic state, reflected in its smallest spatial extent compared to the other archetypes and the presence of the weak Icelandic Low, which is present only in this pattern. The vertical motion field is consistent with the 500-mb geopotential height field, specifically with upward vertical motion accompanying regions of positive differential vorticity advection downstream of the trough axis. EIS exhibits a tongue of low values oriented from southwest to northeast, with smaller values equatorward and to the west. This tongue of low EIS values is present during June in all of the dominant states, and fine details in the position and magnitude of this EIS tongue is consistent with the vertical motion field. Specifically, areas of strong subsidence at 500-mb are associated with greater stability and a westward displacement of the low-EIS tongue. In the pre-trough state, the Azores experience low values of EIS and lie on the border between upward and downward vertical motion at 500-mb, depending on the location of the trough axis at 500-mb.

The trough pattern shows a weak positively tilted 500-mb trough located over and to the southwest of the Azores. The 500-mb trough is evidently not sufficiently strong to promote development of a surface low, but the pattern exhibits a weaker low-level Bermuda High compared to the post-trough and ridge regimes. The weak trough does not exhibit the robust region of ascent down- stream of the trough axis as in the pre-trough pattern. Subsidence is widespread in this state, which encourages greater stability values across the northern and eastern portions of the domain (with the exception of the most northwestern portion of the domain, which is strongly influenced by extremely cold waters that enhances stability in the area). Over the Azores, both the trough and pre-trough patterns exhibit similar EIS values.

The post-trough pattern shows the 500-mb trough axis on the far eastern portion of the domain, with the Azores just east of a ridge axis. The Bermuda High is strong at this state, and is co-located with the 500-mb ridge axis. The tongue of low stability is restricted to the western-most portion of the domain. The strongest subsidence is found in this synoptic state, with a maximum located downstream of the 500-mb ridge axis. This strong subsidence promotes larger EIS values over the Azores compared to the pre-trough and trough states, making this the most stable synoptic state experienced by the Azores region. A small region of low-EIS values is associated with the trough axis on the easternmost region of the domain.

The ridge pattern exhibits the greatest 500-mb heights, with the ridge axis centered over the Azores. The Bermuda High at 1000-mb is similar in structure to that in the post-trough state, but the high-pressure system is more centered over the Azores and does not extend as far north. Subsidence dominates much of the southern portion of the domain, with a maximum downstream of the ridge axis. The EIS structure in the ridge regime is similar to the post-trough state, but the eastern potion of the domain is dominated by larger EIS values, likely because of more widespread subsidence leading to stronger stability. The Azores lie along a west-east gradient in stability, as they do in the post-trough state.

Figure 4 shows the characteristic cloud patterns for the dominant June synoptic states. We employ total condensate (the sum of liquid water path and ice water path, LWP+IWP) from ERA–I, total cloud fraction from ERA–I and MODIS, and cloud top temperature from ERA–I and MODIS to explore the cloud behavior accompanying the four dominant synoptic regimes. Projections of MODIS and ERA–I cloud fraction onto the SOM nodes illustrate the mean spatial distribution of cloud cover for each node. Because of differences in how cloud overlap assumptions between the MODIS liquid water cloud fraction and the low-cloud fraction calculated from ERA–I, the two are not compatible. We instead focus on total cloud fraction and CTT, also considering total condensate as another measure of cloud properties characterized by the reanalysis. Figure 7 indicates that the ERA–I cloud fraction is systematically smaller than cloud fraction estimates from MODIS, but patterns of cloud fraction and CTT are often in reasonable agreement.

In the pre-trough state, the Azores lie within a strong gradient (NW–SE) in condensate and cloud fraction, with both quantities increasing toward the north- west. These cloud structures lie downstream of the trough axis in Fig. 3 and appear to be associated with areas of strong upward vertical motion. On average, these are mixed-phase clouds (CTT < 250 K). Condensate and cloud fraction decrease substantially toward the south and southeast, except for a small tongue of larger cloud fraction east and southeast of the Azores. This area of warm, low cloud (stratocumulus, most likely) is evident in both the MODIS data and reanalysis. These low clouds lie in an area of subsidence and modestly stable values of EIS (~4–5 K). In this regime, the Azores lie near the strongest part of the gradient in cloud fraction and CTT, and therefore may experience either low-altitude liquid stratocumulus or higher-altitude frontal clouds associated with synoptic systems influencing the region. The trough pattern shows colder cloud tops displaced toward the south and southeast portions of the domain. In this regime, the Azores lie well inside the synoptic cloud shield. The steepest gradient in ERA–I condensate, cloud fraction, and CTT is less evident in the MODIS cloud fields, which display a less coherent signal. In fact, the MODIS retrievals exhibit a substantial northward intrusion of warm cloud tops (low clouds) that in the reanalysis is present only over the easternmost portion of the domain.

In the post-trough state, total condensate is more extensive over the southern portion of the domain than in pre-trough and trough states. The area of strong subsidence in Figure 6 and low CTTs for this pattern indicates that the majority of the clouds over and to the east, south and southwest of the Azores are stratocumulus clouds. The spatial configuration of ERA–I and MODIS cloud fractions are quite similar in this regime. These stratocumulus are found downstream of the 500-mb ridge axis and over the eastern portion of the Bermuda High, in a region of stronger EIS values. The areas of maximum total condensate, and ERA–I and MODIS cloud fraction are collocated with areas of ascent in the northwestern portion of the domain and do not reach as far south as in the pre-trough state. The warm cloud tops indicate that stratocumulus are the dominant cloud type over the Azores in the post-trough state.

Because of the strong gradient in vertical motion and strong subsidence downstream of the 500-mb ridge axis (Fig. 6), the ridge pattern most clearly illustrates the different cloud regimes in the region. The area of ascent at 500-mb in the far northwest is associated with condensate values as high as 200 g m^{-2}. The clouds associated with this total condensate are cold (~260 K for both MODIS and reanalysis) and spatially extensive, with their boundary in the vicinity of the Azores. North of the Azores, the cloud field transitions to warmer (i.e., lower) cloud. This stratocumulus deck is encouraged by the subsidence maximum in this state, and lies in an area of stronger stability. Stratocumulus is the most extensive in this ridge pattern, which may be attributed to such high values of subsidence downstream of the ridge axis. In this regime, cloud conditions at the Azores are influenced by the southeastern stratocumulus deck and the relatively clear slot to the southwest, which may modulate the Azores cloud field. The overlapping of the regimes suggests an environment conducive to substantial variability in cloud properties at the Azores.

We characterize the annual cycle of synoptic regimes by applying the SOM analysis to anomalies for each month calculated as described above, and then classifying the nodes into pre-trough, trough, post-trough, ridge, or zonal categories. This exercise results in the annual cycle shown in Fig. 5a, which indicates that all the different synoptic configurations are present in each month. Particularly noteworthy is the result that June experiences synoptic intrusions (trough regimes) 20.5% of the time, a frequency greater than what might be expected given the dominant Bermuda High in the summertime months. This breakdown using month-by-month classifications accurately reflects the synoptic variability at any given time relative to what typically occurs in that month. We note, of course, that the trough classification in January is substantially different (much stronger) than the June trough classification.

Performing the SOM analysis using anomalies based on the annual mean and standard deviation results in only a single classification (trough, pre-trough, etc.) for the entire annual cycle. In this approach, the trough classification is characteristic of the strong troughs present during the winter, and the ridge classification represents conditions of the summertime Bermuda High. For this reason, summer is dominated by ridge and zonal patterns, whereas winter is predominately trough and post-trough type patterns (Fig. 5b). This annual perspective of the data set (Fig. 5b) does not exhibit the trough classification during the summer months and therefore misses the synoptic intrusions identified in the monthly analysis shown in Fig. 5a. Similarly, these “annual” anomalies indicate that the winter months are dominated almost exclusively by trough and post-trough weather patterns, without any ridge features. Fig. 5a shows, on the other hand, that ridges are clearly present in the wintertime months.

The differences in these two approaches lie in how the classifications are defined. Using only a single SOM node space for the entire year means that winter months will tend to map to more trough-like nodes, and summer months will map to more ridge-like nodes. Our analysis focuses on synoptic variability, and therefore anomalies based on monthly means will better characterize how any given synoptic state compares to climatological behavior in its given month.

Insights from modeling and observational evaluation of a cloud-regime transition during MC3E

A case of shallow cumulus and precipitating cumulus congestus sampled at the Atmospheric Radiation Measurement Program Southern Great Plains supersite during the Midlatitude Continental Convective Clouds Experiment is analyzed using a multisensor observational approach and numerical simulation. Observations from a new radar suite surrounding the facility are used to characterize the evolving statistical behavior of the precipitating cloud system. This is accomplished using distributions of different measures of cloud geometry and precipitation properties. Large-eddy simulation (LES) with size-resolved (bin) microphysics is employed to determine the forcings most important in producing the salient aspects of the cloud system captured in the radar observations. Our emphasis is on assessing the importance of time-varying versus steady state large-scale forcing on the model's ability to reproduce the evolutionary behavior of the cloud system. Additional consideration is given to how the characteristic spatial scale and homogeneity of the forcing imposed on the simulation influences the evolution of cloud system properties. Results indicate that several new scanning radar estimates such as distributions of cloud top are useful to differentiate the value of time-varying (or at least temporally well-matched) forcing on LES solution fidelity.

Cloud fraction observations and simulation results are summarized in Fig. 6. The different observational CF estimates are consistent (~70–90% CF) over the later period, when congestus were present. A significant spread in estimates was observed during the shallow cumulus period prior to precipitation onset (~10–90% CF). The VISST satellite-based product ("GOES low+med" in Fig. 6) estimated the largest CF, with a sizeable component of this CF value attributed to mid-to-upper level clouds (~8 km altitude) wrapping into the northern sections of the domain. The CF values estimated by narrower field-of-view ARM sensors (TSI, SIRS, and ARSCL) were consistent with campaign visual reports of scattered low cumulus transitioning to a more overcast cloud field populated by congestus. The SACR CF estimate adopted by this study was unavailable prior to 1830 UTC, and when available reported the lowest CF values when congestus were present (~60%). TSI and satellite images indicate that the discrepancy is partially the consequence of directional sampling limitations. Specifically, the SACR scanning prioritized a direction along the prevailing northwesterly wind such that half of the radar RHI was performed toward the southeast, the region least favorable for cloud development.

For the early cloud period, all LES solutions ostensibly overestimated CF (Fig. 6, gray and black shading and control lines) compared to the median observational estimate of 0.49 calculated from 1500 to 1800 UTC. Comparisons with CF observations suggest the most credible shallow cumulus representation was obtained when applying time-varying forcing conditions initiated at 1200 UTC (1200v_75, 1200v_150). These two forcing configurations include the constraints that we expected would best capture the time-evolution of cloud system properties for this challenging transition event. A reversal in model–observation CF characteristics was observed following precipitation onset, with the ensemble members underpredicting the CF associated with the congestus mode as compared to the observational consensus. One noteworthy exception was the 2100s_75 simulation that predicted extensive cloud coverage associated with low-topped cumulus (cloud top heights of ~3 km). The time-evolving forcing configurations, and the steady-state configurations corresponding to the times when congestus were present, typically resulted in higher CF values and better agreement with CF observations during the late-

event period. Beyond 9 hours, several of the steady-state runs trend toward a domain-limited behavior of a few prominent cloudy cells.

The usefulness of CF comparisons beyond this basic qualitative agreement is not clear. Cloud fraction is an important quantity via its influence on the radiation budget, and therefore it constitutes a bulk measure of the cloud system that models should strive to simulate. However, as a tool for diagnosing model pathologies (i.e., the root cause of model–observation mismatch and how to fix it), CF is inadequate. Furthermore, the SAMEX modeling framework is highly idealized and assumes horizontally homogeneous initial conditions and forcing. For this study, the prevailing forcing of positive moisture advection and negative potential temperature advection is conducive to simulating the observed transition from shallow clouds to a field that includes both shallow cumulus and congestus. The homogeneity of forcing, however, dictates that clouds initiate with an equal likelihood everywhere within our LES domain. In other words, cloud behavior is statistically homogeneous across the model domain, in contrast to the highly variable spatial structure present in the satellite and radar imagery. The SACR observations, on the other hand, indicate a cloud population that is not statistically homogeneous. For this reason, CF metrics between the statistically homogeneous simulations and the horizontally heterogeneous observational cloud field may differ substantially.

During the later period when congestus are present, LES CF values are closer to the observations (median value of 0.85 from 1800 to 2100 UTC). Based on similar arguments as above, this agreement may be fortuitous. We note that LES solutions progress towards stronger isolated congestus reminiscent of the deep precipitating congestus clouds sampled by the C-SAPR. However, the LES behavior of a simple evolution from shallow cumulus to isolated deeper congestus conflicts with the complexity found in the ARM CF observations that favor the coexistence of a spectrum of cloud depths; these include the deep, strongly precipitating congestus, and also weaker congestus elements and commingled shallow cumulus clouds. Although we cannot address this discrepancy with certainty, we speculate that the differences may arise from the highly idealized nature of the forcing, particularly in two respects: First, since the piecewise continuous forcing is applied at three-hour intervals, we should not necessarily expect the model to reproduce fine-scale cloud behavior in time. Second, the forcing profiles and doubly periodic boundary conditions impose an assumption of statistical homogeneity across the simulation domain, whereas the observed transient cloud system exhibits substantial horizontal variability over the same scale.

A snapshot of the model-generated radar reflectivity field for the 1200v_75 control simulation at 1500 UTC shows an array of shallow cumulus, deeper cumulus clouds, and strongly precipitating cumulus congestus (Fig. 7). LES cloud-field median and 90th percentile tops (not shown) for all simulations were consistent with SACR and ARSCL observations of the tail end of distributions of shallow cumulus transitioning to later congestus. The 90th percentile values typically range from top heights less than 4 km early, to heights of 5.5–6 km at later stages. In this simple manner, the two-dimensional SACR observations are immediately useful for providing a more realistic range for cloud top and bottom heights as compared to traditional column-based radar observations. Further, SACR time series depictions of the cloud top distributions provide additional support for scrutinizing the evolution of LES cloud fields. For this event, the results emphasize the benefits of forcing that closely mimics observations (either time-varying or well-matched to the observational period of interest). For example, the most accurate depiction of the cloud top distribution is found when using the time-varying forcing (1200v_75, 1200v_150). These

simulations properly capture the bimodal cloud top features in the observations and suitably delay the initiation of significant congestus to better match with precipitation onset timing (see the precipitation onset lines in Fig. 8 and the evolution of precipitating echo area [not shown]). The 1500 UTC and 1800 UTC steady-state forcings also developed bimodal cloud top behaviors (Fig. 8) characteristic of those observation times. The reason for the bimodal cloud behavior is not clear, but preliminary analysis suggests that variations in low-level stability may lead to differences in cloud depth, precipitation initiation, and subsequent cloud-system behavior. The early steady-state forcing conditions (1200 UTC) preclude rapid development of precipitating congestus, whereas using later steady-state forcing (2100 UTC) results in a cloud population with characteristic tops inconsistent with observations (e.g., Fig. 8). Although SACR insights are beneficial, the limits of the SACR scanning strategy employed for the 25 May 2011 case suggests that additional radars and scanning modes are required to fully characterize three-dimensional distributions of cloud properties.

Microphysical precursor conditions leading to precipitation initiation in marine stratocumulus

Although the classical model of how a population of cloud droplets grows to precipitation-sized drops through the condensation and coalescence processes is well accepted, it does not fully address the history of how nascent precipitation drops come about in warm clouds. A size-resolving (bin) large-eddy simulation (LES) model and a parcel trajectory model are used to investigate the dominant microphysical precursor conditions influencing precipitation initiation for a case of marine stratocumulus based on conditions sampled during the CAP-MBL field campaign in the eastern North Atlantic. Backward trajectories are then calculated beginning from ten regions of nascent precipitation to analyze the precursor conditions of precipitation onset. A suite of backward trajectories is also calculated from ten null cases originating in regions that do not form drizzle.

The backward trajectories originating in nascent drizzle regions exhibit larger mean cloud droplet radius (r_v) relative to the null cases, as would be expected since larger cloud droplets tend to preferentially form drizzle. These nascent drizzle cases experience anomalously low droplet concentration (N_c) along the trajectory path, relative to the null cases, but also low values of cloud-water mixing ratio (q_c). These results indicate the most surprising aspect of our study, specifically that the larger values of mean volume radius (r_v) are driven, not by large cloud liquid water contents (q_c), but rather by small values of cloud droplet concentration (N_c). These findings suggest that new regions of drizzle are associated with parcels that previously participated in the drizzle process.

The contours in Fig. 9 are cross sections from the LES results representing the conditions of Z, q_r, q_c, and N_c for the center location of the trajectory volume in the nascent drizzle cell. From this time, the trajectories are integrated backward in time. To minimize confusion, we consistently describe trajectory movement through time in a typical, forward-in-time fashion. The backward trajectories from regions of precipitation initiation exhibit three distinct characteristic behaviors. The first characteristic (CB, cloud base) has the majority of trajectories moving from below or near cloud base and into the cloud as they become the sampled cell (four cases). With the second characteristic (CT, cloud top), the majority of trajectories begin higher in the cloud and fall lower in the cloud before moving horizontally as they

become the sampled cell (two cases). The third characteristic (CA, all cloud) is a combination of CB and CT (four cases). Fig. 9 shows examples of CB, CT, and CA trajectory behaviors.

As mentioned before and evident in Fig. 9, all cases are initialized in regions of the contour $0.01 \leq q_r \leq 0.055$ g kg^{-1}, though most trajectories end in regions where $q_r \leq 0.025$ g kg^{-1} (not shown). Fig. 9 depicts the majority of trajectories ending in regions with lower reflectivities and N_c values, specifically where $Z < 0.0$ dBz and $N_c < 60.0$ cm^{-3}. In some cases, the trajectories are initialized near regions of high N_c concentrations, as seen in Case 3 (Fig. 9). Also, considering the homogeneous nature of q_c, most trajectories end in regions where 0.1 g kg^{-1} $\leq q_c \leq$ 0.5 g kg^{-1}.

Fig. 9 demonstrates the distinct behavior of the trajectory ensembles for the three example cases. Most CB cases begin with all trajectories lying in the subcloud layer, and in the example CB case 75% of the trajectories reach the cloud within 10-15 minutes. By 17 minutes, all trajectories are inside the cloud. The mean volume radius of droplets in the cloud spectrum r_v is included in our analysis because of the importance of large droplets to precipitation initiation. The variables r_v, q_r, and q_c are not conservative thermodynamic variables, and as such we do not expect them to remain constant along a trajectory. The behavior of average trajectory r_v for the example CB case (not shown) increases through time as the trajectories rise in the cloud and capture the production of embryonic drizzle droplets. The trajectories' in-cloud ($q_c > 0.01$ g kg^{-1}) q_c values are consistent with vertical ascent through increasing adiabatic liquid water content values. The behavior of the trajectory N_c values in the cloud spectrum for the CB case is somewhat noisy early in the trajectory calculation because of the small number of trajectories in the cloud. As more trajectories enter into the cloud, average trajectory N_c remains fairly constant or increases slightly, staying mostly in the range of 40 cm^{-3} $\leq N_c \leq$ 60 cm^{-3}. This behavior is expected as N_c should be well conserved in droplets that reside inside the cloud and away from supersaturated regions of droplet nucleation.

Fig. 10 compares mean PDFs of r_v, q_r, q_c, and N_c composited from the entire 20-minute trajectory calculation for both the P and N cases. PDFs are calculated only for when the trajectories reside in the cloud ($q_c \geq 0.01$ g kg^{-1}). These 20-minute PDFs can in some sense be interpreted as a time-integral of the properties along the trajectories for the entire 20-minute trajectory calculation. The breadth of these PDFs indicate the conditions the droplets experience from the beginning of the trajectory calculation up through the time of the nascent drizzle cell. We compare the P and N PDFs of each variable not only to ensure that the P cases we use are dissimilar to the N cases and consequently not initialized too early but also to determine whether N_c or q_c more strongly governs precipitation initiation. The r_v distributions for both P and N categories appear similar. However, the secondary peak in the P distribution around 12 μm along with the longer tail ($r_v > 14$ μm) signifies the parcels in the P cases contain larger droplets that will eventually become nascent drizzle, whereas the majority of parcels in the N cases stop growing after they reach ~10 μm.

It is also clear that the P and N PDF distributions for q_r, q_c, and N_c differ greatly. As to be expected, the N q_r PDF peaks very close to 0.0 g kg^{-1}, much lower than the P PDF, as these are non-precipitating cases. The tail of larger N values is associated with the few outlier trajectories that may briefly move through small cells of higher q_r values. P N_c peaks at 50 cm^{-3}, much lower than the N's peak around 110 cm^{-3}. P q_c also peaks much lower than the N, with a peak near 0.1 g kg^{-1} compared to a peak of ~0.45 g kg^{-1}. These

are surprising results that do not match our initial hypothesis that precipitation initiation would be driven largely by larger values of liquid water content.

We calculate multiple statistical measures to determine whether differences between the P and N distributions are statistically significant. We use the Welch's t-test assuming unequal variances to test the significance of the differences in the means of the P and N PDFs, and the F-test to determine the significance of the differences in variance of the P and N PDFs. The q_r, q_c, and N_c means are statistically significant at the $\alpha = 0.05$ significance level. Differences in N_c and q_r variances are significant as well. To more completely evaluate differences in the PDFs, we also apply the Kolvogorov-Smirnoff test (Appendix B) to the cumulative density functions (Fig. 15) of the P and N trajectory PDFs. This test reports that the differences in the r_v and q_c CDF's are also statistically significant at the $\alpha = 0.05$ significance level.

Summary Highlights of the KU contributions to the collaborative research

- Employed the artificial neural net technique of self-organizing maps to characterize the variability of synoptic conditions and cloud properties over the northeast Atlantic (M.S. student Carly Wittman)
- Performed a systematic comparison between LES model and observations of a transitioning cloud case sampled in MC3E to evaluate the sensitivity of model results to initial conditions (collaboration with Scott Giangrande at Brookhaven National Laboratory)
- Explored precursor conditions for precipitation initiation in marine stratocumulus (M.S. student Hannah Chandler)
- Quantified the behavior of the relationship between cloud amount and environmental parameters as a function of scale.

FIGURES

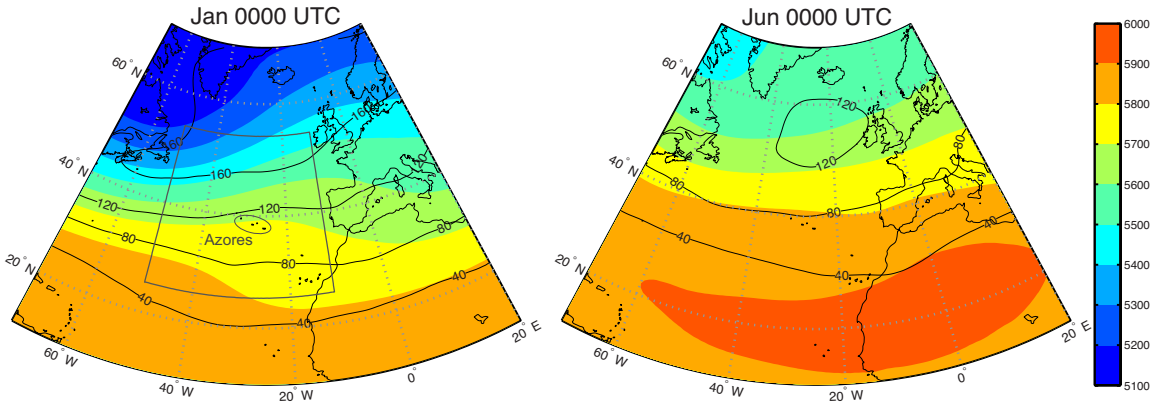

Figure 1: Mean 500-mb heights for January and June. The inner box in the left map represents the smaller domain used to analyze variability in the vicinity of the Azores. Black contour lines are standard deviation of the mean 500-mb height, and can be used as a proxy for storm track variability, where higher numbers indicate greater variability.

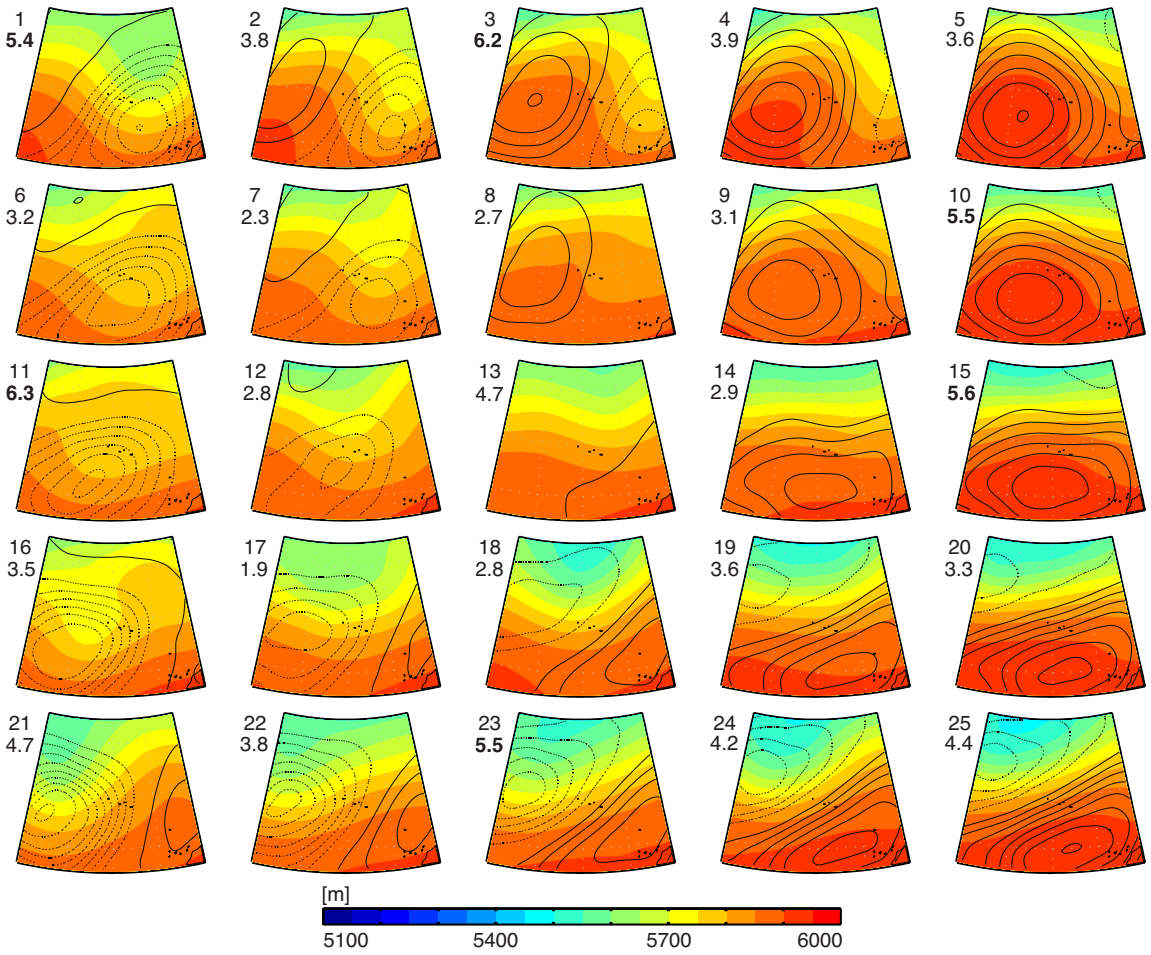

Figure 2: SOM nodes of 500-mb geopotential heights with overlaid contours of normalized 500-mb geopotential height anomalies for June. The numbers in the upper left-hand portion of each node indicate node number and the relative frequency of occurrence of each node. Bold frequency values represent statistically significant nodes based on a 95% confidence interval using the method of Schuenemann et al. (2009).

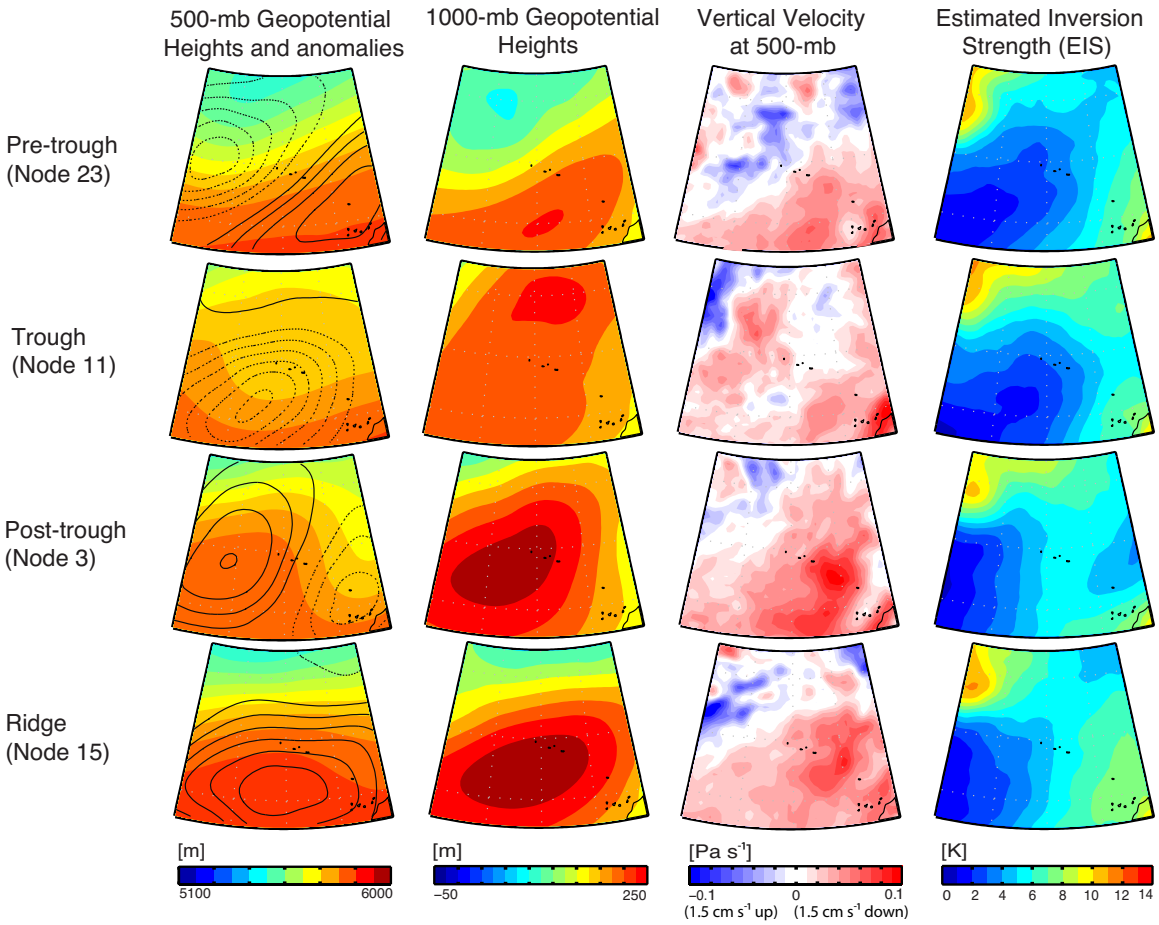

Figure 3: Synoptic properties for the four archetypal synoptic regimes in June, including 500-mb geopotential heights and anomalies, 1000-mb geopotential height, 500-mb vertical velocity, and estimated inversion strength.

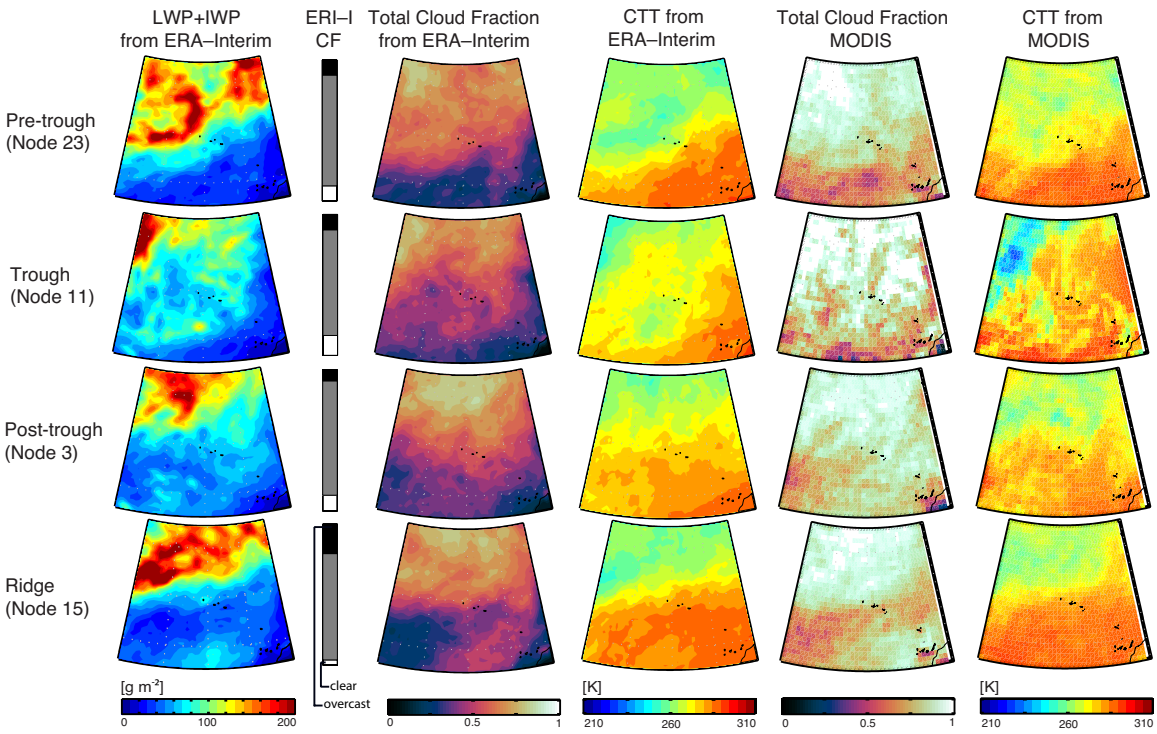

Figure 4. Cloud properties for the four archetypal synoptic regimes in June. For each regime, fields plotted are total ERA–I condensate, total cloud fraction, and cloud-top temperature, and total cloud fraction and cloud-top temperature from MODIS.

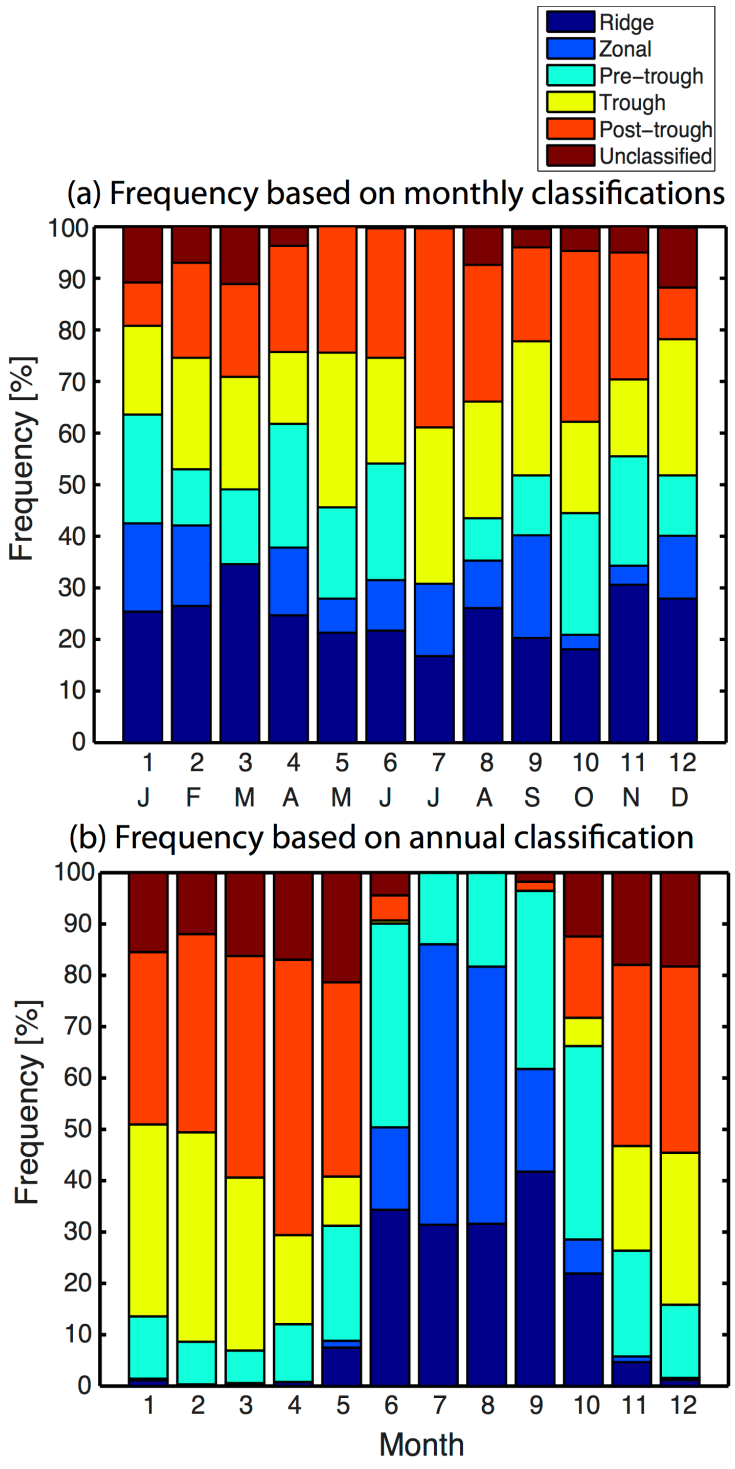

Figure 5. Annual cycle of ridge, zonal, pre-trough, trough, post-trough and unclassified patterns based on the anomalies calculated using (a) monthly averaging windows; or (b) a window the length of the full dataset.

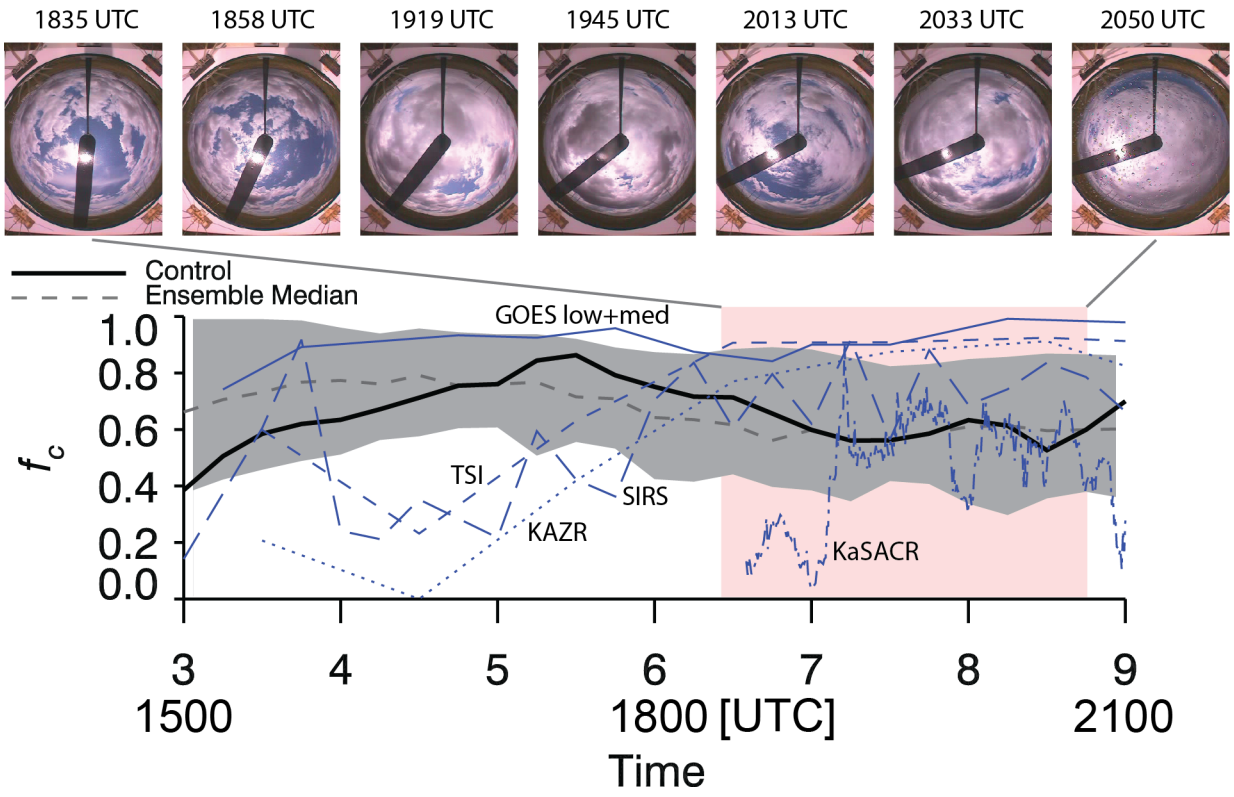

Figure 6: A series of imagery from the total sky imager (TSI, top). Five observational estimates of cloud fraction, all denoted by blue lines overlaid on cloud fraction calculated from the simulation suite (bottom). The black line represents the control (1200v_75) simulation. The dashed gray line is the ensemble median, and the gray bands represent the minimum and maximum cloud fraction values of the simulation ensemble. The rose shaded area indicates the period covered by the TSI images.

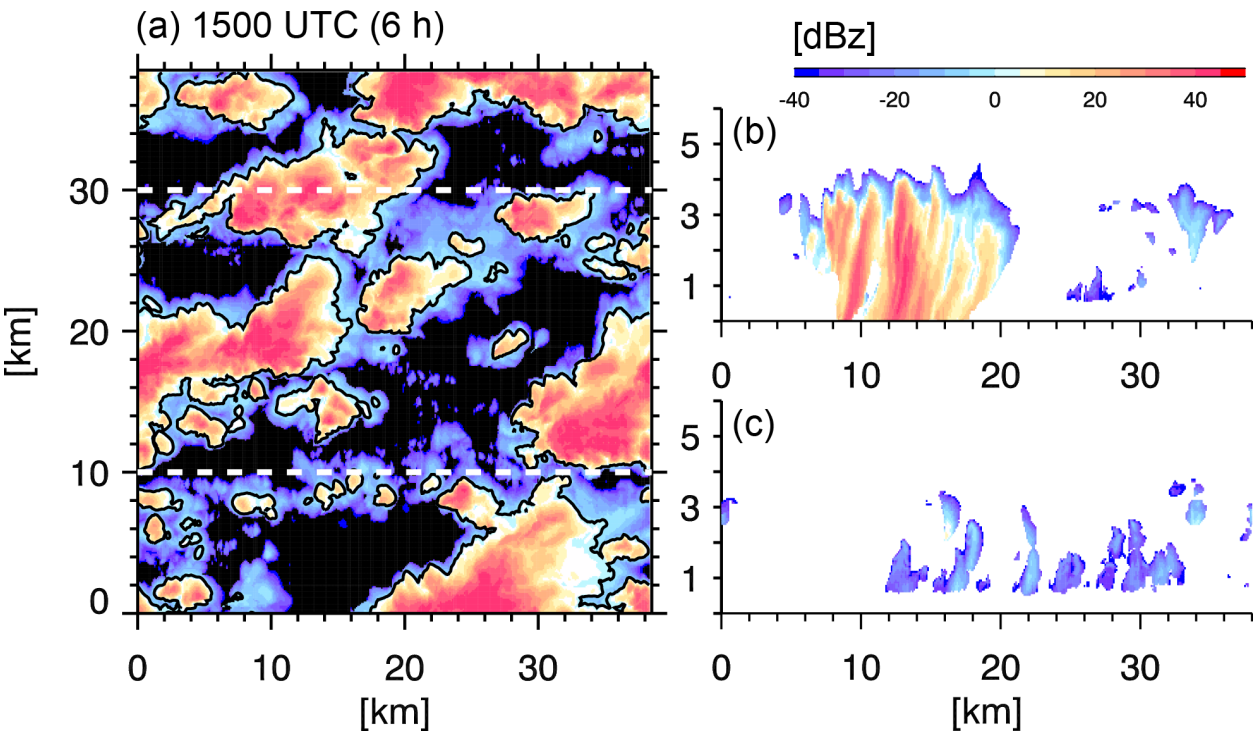

Figure 7: Snapshot of the simulated reflectivity field from the 1200v_75 control simulation, calculated directly from the bin-microphysics drop size distributions. (a) Plan view of column-maximum reflectivity. Solid black contours are 0 dB*z*, representative of typical C-band radar sensitivity. (b) and (c) represent vertical cross sections taken through the northern and southern regions of the domain in (a).

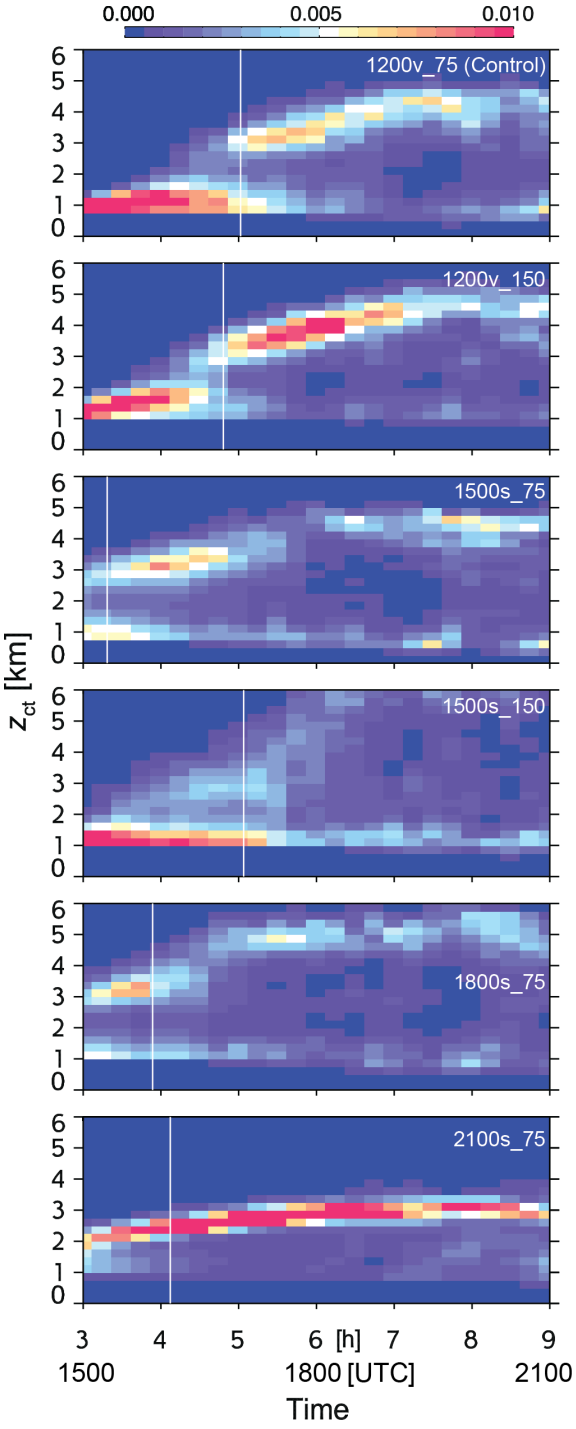

Figure 8. Time-varying PDFs of cloud-top height for six of the simulations. The white line represents the time of precipitation onset, taken to be a precipitation rate of 1 mm d^{-1} at the surface.

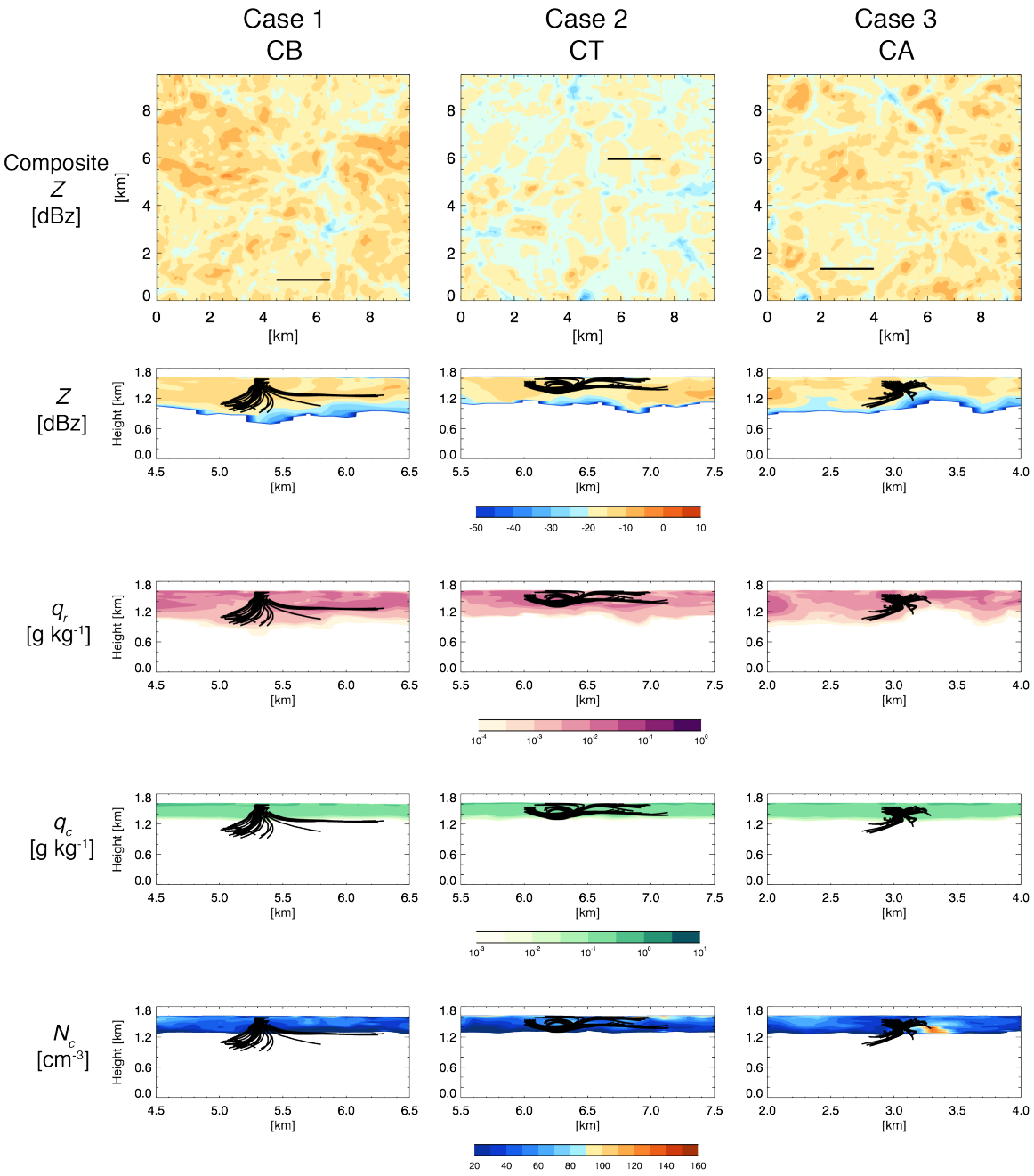

Figure 9: Composite simulated reflectivity and vertical cross sections of simulated reflectivity, q_r, q_c, and N_c at the trajectory model initialization time and median trajectory initialization location for 3 example cases of characteristic trajectory behavior. 30 trajectory paths are overlayed to show a representation of the characteristic behavior of the trajectories in each case. The cross sections are plotted at the black lines overlayed on composite simulated reflectivity for each case.

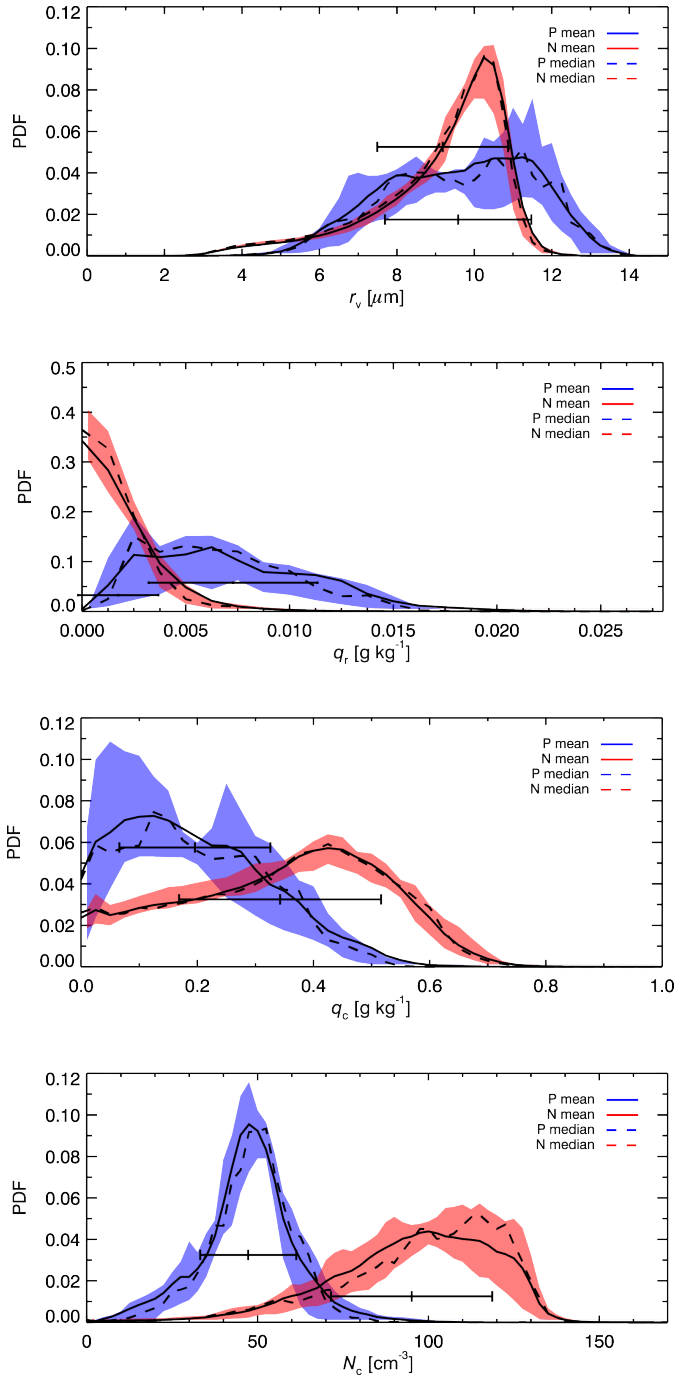

Fig. 10. Normalized averaged frequency distributions (PDFs) of all P and N cases taken from the entire 20-minute trajectory calculations for mean volume radius of the cloud spectrum r_v, rain water mixing ratio q_r, cloud water content q_c, and cloud drop concentration of the cloud spectrum N_c. Whiskers represent the mean (middle vertical line) and 1 standard deviation (outside vertical lines).

Project Participants:

Faculty:
Dr. David Mechem, University of Kansas
Dr. Simon de Szoeke, Oregon State University
Dr. Sandra Yuter, North Carolina State University

University of Kansas Graduate Students:
Carly (Fish) Wittman, M.S. Atmospheric Science
Hannah Chandler, M.S. Atmospheric Science

Peer-reviewed Publications

[These are publications in print that are directly related to the grant. Three additional manuscripts related to the project are in preparation for submission in the next year.]

Kogan, Y. L., **D. B. Mechem**, and K. Choi, 2012: Effects of sea-salt aerosols on precipitation in simulations of shallow cumulus. *J. Atmos. Sci.*, 69, 463–483.

Mechem, D. B., and A. J. Oberthaler, 2013: Numerical simulation of tropical cumulus congestus during TOGA COARE. *J. Adv. Model. Earth Syst.*, **5**, 1-15, doi:10.1002/jame.20043.

Kogan, Y. L., and **D. B. Mechem**, 2014: A PDF-based microphysics parameterization for shallow cumulus clouds. *J. Atmos. Sci.*, 69, 1070–1089.

Mechem, D. B., S. E. Giangrande, C. S. Wittman, P. Borque, T. Toto, and P. Kollias, 2015: Insights from modeling and observational evaluation of a precipitating continental cumulus event observed during the MC3E field campaign. *J. Geophys. Res. Atmos.*, **120**, 1980–1995, doi:10.1002/2014JD022255.

Wood, R., M. Wyant, C. S. Bretherton, J. Remillard, P. Kollias, J. Fletcher, J. Stemmler, S. de Szoeke, S. E. Yuter, M. Miller, **D. Mechem**, G. Tselioudis, C. Chiu, J. Mann, E. O'Connor, R. Hogan, X. Dong, M. Miller, V. Ghate, A. Jefferson, Q. Min, P. Minnis, R. Palinkonda, B. Albrecht, E. Luke, C. Hannay, and Y. Lin, 2015: Clouds, aerosol, and precipitation in the marine boundary layer: An ARM Mobile Facility deployment. *Bull. Amer. Meteor. Soc.*, **96**, 419–440.

de Szoeke, S. P., K. L. Verlinden, S. E. Yuter, and **D. B. Mechem**, 2016: The time scales of variability of marine low clouds. *J. Climate*, **29**, 6463–6481.

Kogan, Y. L., and **D. B. Mechem**, 2016: A PDF-based formulation of microphysical variability in cumulus congestus clouds. *J. Atmos. Sci.*, **73**, 167–184.